Solar Energy 198 (2020) 529–534

Contents lists available at ScienceDirect

Solar Energy

journal homepage: www.elsevier.com/locate/solener

Effect of annealing temperature of MoO_3 layer in MoO_3/Au/MoO_3 (MAM) coated PbS QDs sensitized ZnO nanorods/FTO glass solar cell

Hamid Latif[a,*], Rabia Zahid[a], Saba Rasheed[a], Abdul Sattar[b], M. Shahid Rafique[c], S. Zaheer[a], Syeda Ammara Shabbir[a], K. Javed[a], Arslan Usman[b], R.J. Amjad[b], S. Malik[d], Shaziab Khurshid[a]

[a] Department of Physics, Forman Christian College, Lahore, Pakistan
[b] Physics Department, COMSATS University Islamabad, Lahore Campus, Lahore, Pakistan
[c] Department of Physics, University of Engineering and Technology, Lahore, Pakistan
[d] Department of Mathematics, Forman Christian College, Lahore, Pakistan

ARTICLE INFO

Keywords:
Quantum dots
ZnO nanorods
PbS quantum dot sensitized Solar Cell
MoO_3 thin film

ABSTRACT

This research reports fabrication of MoO_3/Au/MoO_3 (MAM) coated PbS sensitized quantum dot solar cell. ZnO nanorod grown FTO glass substrates were sensitized by PbS quantum dots (PbS QDs/ZnO nanorods/FTO Glass), followed by (MoO_3/Au/MoO_3) coating. Hydrothermal process was used to grow ZnO nanorods, followed by the deposition of PbS QDs using Successive Ionic Layer Adsorption and Reaction (SILAR). Finally, (MoO_3/Au/MoO_3) layers were deposited for the back contact. Spin coating was used to deposit MoO_3 layers while middle layer of Au was deposited by sputter coating. Three such devices were fabricated with three different annealing temperatures i.e. 100 °C, 150 °C and 200 °C for first MoO_3 layer. Scanning Electron Microscopy (SEM) was used for surface morphology of the devices; Energy Dispersive Spectroscopy Analysis (EDS) and X-Ray Diffraction (XRD) techniques were used for elemental and structural analysis, Optical properties of the devices were determined using UV–Visible analysis. Power conversion efficiency (PCE) of all three devices was obtained to observe devices performance. Improved PCE of 4.617% was obtained by the device with the thermal treatment of 150 °C.

1. Introduction

Solar cells are one of the most utilized solar energy technologies that provide both the scalability and the technological maturity to fulfill the world-wide demand for electricity. In the past few years, a number of thin-film technologies have emerged which promise low-cost, light weight, transparent and flexible designs (Jean et al., 2015; Jo et al., 2017; Kang et al., 2018).

Quantum Dot Solar Cells (QDSCs) are one of the emerging thin-film solar cells that might not be mature enough to be installed widely but their low-cost production, air-stability and low temperature processing techniques predict them to be a promising candidate for the upcoming PV technologies (Samadpour et al., 2019; Rühle et al., 2010; Carey et al., 2015). Much work has been done on QDSCs because of the unique chemical, optical and electronic properties of Quantum Dots (QDs) which are used as a light sensitive material in the QDSCs (Mustakim et al., 2018; Kramer and Sargent, 2011; Lan et al., 2014; Nozik, 2008; Li et al., 2015; Zhang et al., 2014).

For the working electrode, transparent materials are required for the front contact of the solar cell in order to transmit light through it. Fluorine doped tinoxide (FTO) or Tin doped indium oxide (ITO) are commonly used as the Transparent Conducting Oxide (TCO) for the front contact. After that, wide band gap nanostructures like mesoporous films, nanorods, nanowires, nanotubes and nanosheets are used to provide the large surface area for the deposition of QDs. Titanium dioxide (TiO_2) and Zinc Oxide (ZnO) are the most widely used materials. In addition, QDs like CdS, CdSe, PbSe and PbS are used as a light harvesting material of the device. Aqueous polysulfide and organic electrolyte with I^-/I_3^- redox couple are the most commonly used electrolytes in QDSCs which are sandwiched between working electrode and counter electron (Carey et al., 2015). On the other hand, back contacts of metals like Au, Ag and Al have replaced the liquid electrolyte because of their good conductivity and compatibility (Luther et al., 2010; Gao et al., 2011). Furthermore, n-type transition metal oxides like Molybdenum Oxide (MoO_3) are used as a Hole Extraction Layer (HEL) to improve the performance of the device (Gao et al., 2011; Park et al., 2012). An additional MoO3 layer can also be used to improve the transparency of the counter electrode (Zhang et al., 2016; Tao et al., 2009; Yang et al., 2015).

A great many architectures of QDSCs have been proposed over the

* Corresponding author.
E-mail address: hamidlatif@fccollege.edu.pk (H. Latif).

https://doi.org/10.1016/j.solener.2020.01.078
Received 12 September 2019; Received in revised form 25 January 2020; Accepted 28 January 2020

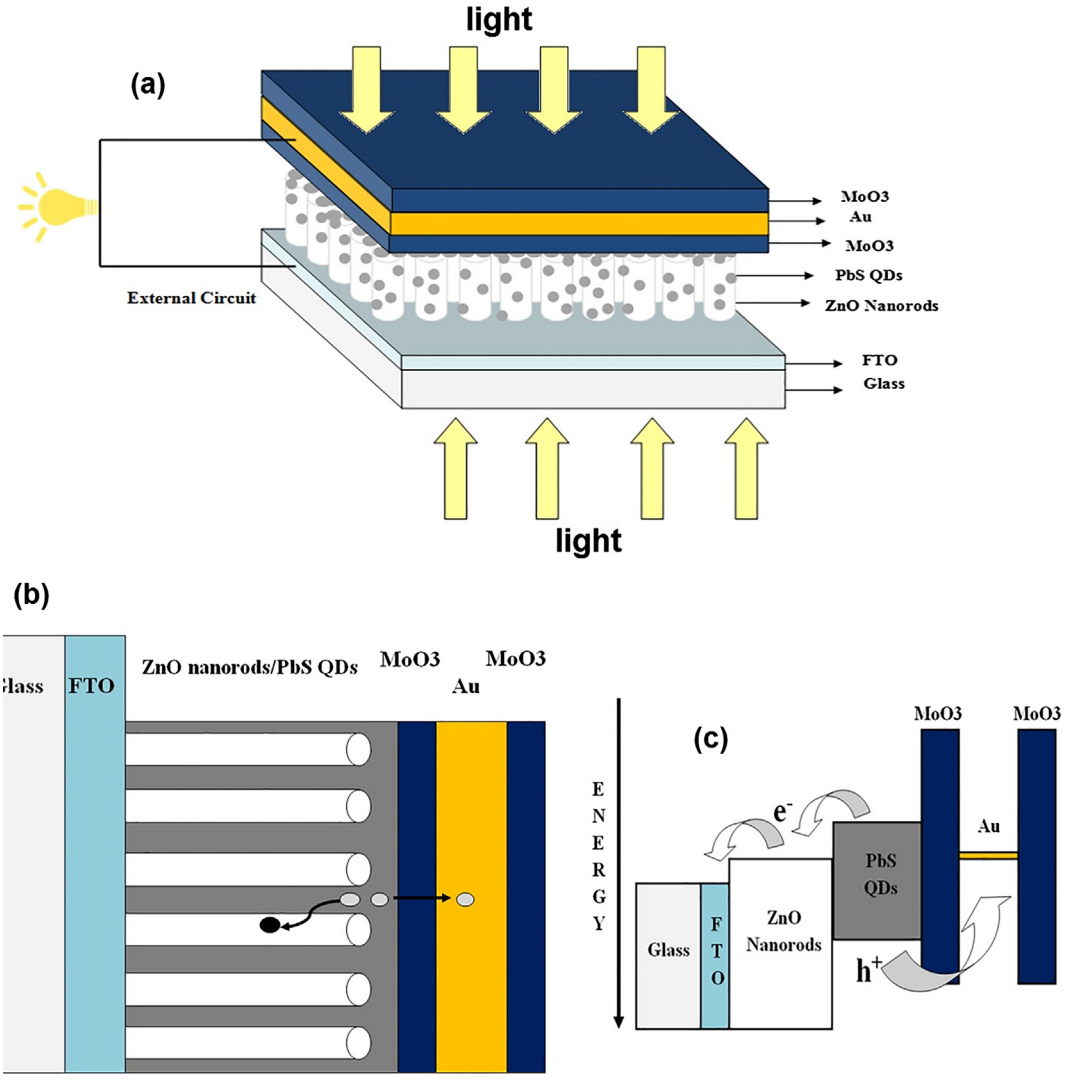

Fig. 1. (a) Device structure of the Quantum Dot Solar Cell (QDSC). (b) 2-D diagram of device. (c) Energy band diagram of the device.

past few years. Herein, a novel architecture of QDSC with MoO_3/Au/MoO_3 (MAM) coated PbS quantum dot sensitized ZnO nanorod is reported (see Fig. 1). As this architecture allowed the fabricated device to be transparent form both sides, hence it can absorb solar radiation from top as well as the bottom. This kind of solar cell can be a promising candidate for space applications. In this device, FTO glass has been used as transparent conducting oxide. On top of that, nanorods of ZnO were grown due to their high electron mobility, adequate surface and easy preparation methods. ZnO nanorods were then sensitized by PbS QDs to serve as a light harvesting layer of the solar cell. In the end, the back contact containing nanolayered MAM was deposited. The annealing temperature of first MoO_3 layer in MAM during the synthesis of the QDSC was changed to 100 °C, 150 °C and 200 °C to fabricate three devices. The schematic of the fabricated device is shown in the figure given below.

2. Experiment

2.1. ZnO nanorods synthesis

ZnO nanorods were grown using the hydrothermal method (Wang et al., 2013; Li et al., 2014; Ibupoto et al., 2013). Firstly, FTO glass was cleaned with deionized water and ethanol respectively by ultrasonic bath. Then, the seed solution was prepared by dissolving Zinc Acetate Dihydrate [Zn $(CH_3COOH)_2 \cdot 2H_2O$] (0.01 M) in ethanol. This seed solution was spin coated on the FTO glass at 3000 rpm for 90 s twice and then the substrate was sintered at 350 °C in furnace for 35 min. This whole process was repeated twice to form a uniform layer. Thereafter, Zinc Nitrate Hexahydrate $Zn(NO_3)_2 \cdot 6H_2O$ (0.02 M) and Hexamethylenetetramine (HMTA) (0.02 M) solution was prepared in deionized water. FTO electrode was vertically dipped in this solution on hotplate at a temperature of 90 °C for 4 h and then dried at 100 °C for 30 min.

2.2. PbS QDs synthesis

PbS QDs were deposited on the ZnO nanorods through SILAR (Tian et al., 2016; Lee et al., 2013). Lead nitrate [Pb $(NO_3)_2$] (0.06 M) and Thiourea (0.3 M) solutions were prepared in deionized water and methanol by the volume ratio 1:1. Firstly, the substrate was dipped in Lead Nitrate solution for 1 min and then rinsed with ethanol for 30 s. Next, immersed for another 1 min in Thiourea on the hotplate at a temperature of 90 °C and again rinsed with ethanol for 30 s. The above series of steps were repeated 20 times for uniform deposition of PbS QDs and the sample was dried at 100 °C for 30 min.

2.3. MAM electrode synthesis

Molybdenum trioxide solution was prepared by forming a

peroxomolydic acid solution (Li et al., 2017). Firstly, MoO_3 powder (0.06 M) was dissolved in ethanediol and isopropanol which were mixed by a volume ratio of 1:9 forming a complex solvent. Then, 30% aqueous Hydrogen Peroxide (H_2O_2) was added to the above solution by a volume ratio of 7:93. A dark blue peroxomolybdic acid solution was formed after ultrasonication for 30 min. Next, peroxomolybdic acid solution was spin coated at 3000 rpm for 40 s, twice on PbS QDs/ZnO nanorods/FTO/Glass. Three samples of MoO_3 on PbS QDs/ZnO nanorods/FTO/Glass were fabricated using the same method. However, they were annealed in the vacuum oven at 100 °C, 150 °C and 200 °C respectively. After that thin-film of Au was sputter coated and the last layer of MoO_3 was deposited by the same method as discussed above on all three samples.

3. Results and discussion

3.1. Structural analysis

The XRD combined pattern of MoO_3/Au/MoO_3 (MAM) coated PbS quantum dots sensitized ZnO nanorod grown FTO glass substrates with first MoO_3 layer annealed at 100 °C , 150 °C and 200 °C for three working electrodes 1, 2 and 3 respectively, are shown in Fig. 2.

From the XRD pattern it is observed that peaks of all relevant materials are present. The peaks of PbS quantum dots for all three samples are observed at 2θ position of 26.31°, 51.30° and 62.71° corresponding to the crystal planes (1 1 1), (3 1 1) and (4 0 0) respectively. It is obvious from the XRD pattern that at angle 34.27° there is a high intensity peak of ZnO with (0 0 2) crystal plane. Two minor diffraction peaks of ZnO for all the three samples are also noticed at 33.54° and 36.12° with crystal planes (1 1 1) and (1 0 1) respectively. The presence of tin oxide is confirmed by diffraction peak at angle 65.33° which is indexed as (1 1 2) crystal plane. The observable peak of molybdenum oxide is detected at 2θ position of 72.42° with crystal plane (7 0 0) and (2 0 0) peak at 43.03° confirms the presence of gold.

XRD analysis reveals that with the increase of temperature the crystallinity of MoO_3 layer increases as the peaks of MoO_3 become sharper. We can observe some crystallinity improvement in PbS as well. The grain size calculated by using Debye Scherrer formula for all the material is given in Table1.

Variation in grain size can be seen from the Table 1. Fig. 3 shows the comparison of grain size of PbS, ZnO, SnO_2 and MoO_3 on sample 1, 2 and 3 for working electrode 1, 2 and 3 respectively.

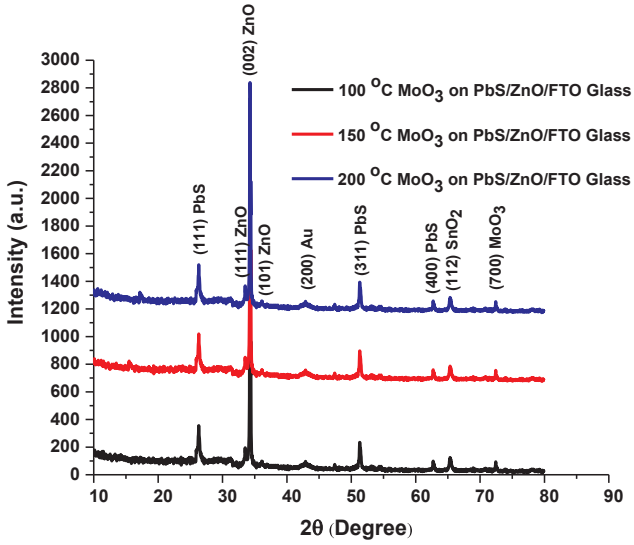

Fig. 2. Combined XRD analysis MoO_3/Au/MoO_3 (MAM) coated, PbS quantum dots sensitized ZnO nanorod grown FTO glass substrates with first MoO_3 layer annealed at 100 °C , 150 °C and 200 °C for three working electrodes, sample1, 2 and 3 respectively.

Table 1
XRD parameters with calculated grain size.

Samples	Material	Position 2θ (degree)	d-spacing (Å)	FWHM (degrees)	Intensity (counts)	Grain size (nm)
Sample 1	PbS	26.31	3.3868	0.1023	356	83.37
Sample 2	PbS	26.36	3.3809	0.1244	278	68.56
Sample 3	PbS	26.35	3.3820	0.1535	364	55.56
Sample 1	ZnO	34.27	2.61666	0.1279	3436	67.94
Sample 2	ZnO	34.26	2.61729	0.0888	1034	97.86
Sample 3	ZnO	34.27	2.61602	0.1279	726	67.94
Sample 1	SnO_2	65.33	1.42834	0.3070	112	32.13
Sample 2	SnO_2	65.36	1.42763	0.1421	111	69.43
Sample 3	SnO_2	65.32	1.42845	0.2558	127	38.57
Sample 1	MoO_3	72.42	1.30392	0.1872	80	54.98
Sample 2	MoO_3	72.44	1.30466	0.0625	41	164.7
Sample 3	MoO_3	72.44	1.30466	0.09	44	114

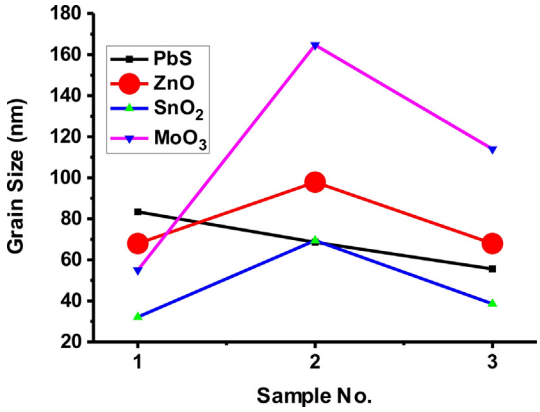

Fig. 3. Comparison of grain size of PbS, ZnO, SnO_2 and MoO_3 for sample 1, 2 and 3 for working electrode 1, 2 and 3 respectively.

The grain size calculated for the high intensity peak of PbS decreases as the temperature increases for sample 2 and sample 3. For the high intensity peak of ZnO the grain size first increases as the temperature of sample 2 increases but for sample 3 it decreases with further increase in temperature. Similar trend is observed for SnO_2 and MoO_3.

All layers except PbS show increase in crystallite size with increase in temperature up 150 °C due to annealing effect. However, MoO_3 shows decrease at higher temperature (sample 3). This decrease could be attributed to the beginning of phase transition from monoclinic which is metastable at ambient conditions; however, at higher temperatures ~200 °C a transition to orthorhombic structure has been reported in literature. (McCarron and Calabrese, 1991; Yao et al., 2012). These variations of decreasing crystallite size may also alter the geometry at interfaces MoO_3/ZnO and ZnO/ITO following similar trend as MoO_3. The strain produced at interface may lead to increase in dislocation density and hence decreasing crystallite structure in both ZnO and ITO (Sun et al., 2018).

On the other hand, PbS quantum dots have much higher surface to volume ration and are more prone to limited oxidation at elevated temperatures, forming PbO and PbSO4. The grain size decreases due to introduction of these impurities which also evident from the decrease in the efficiency of device 3 (Nafees et al., 2017).

3.2. Compositional and morphological analysis

Elemental compositional and morphological analysis has been done using energy dispersive spectroscopy (EDS) and scanning electron microscope (SEM). Fig. 4 shows the EDS micrographs and SEM images along with size distribution of PbS quantum dots of all three working

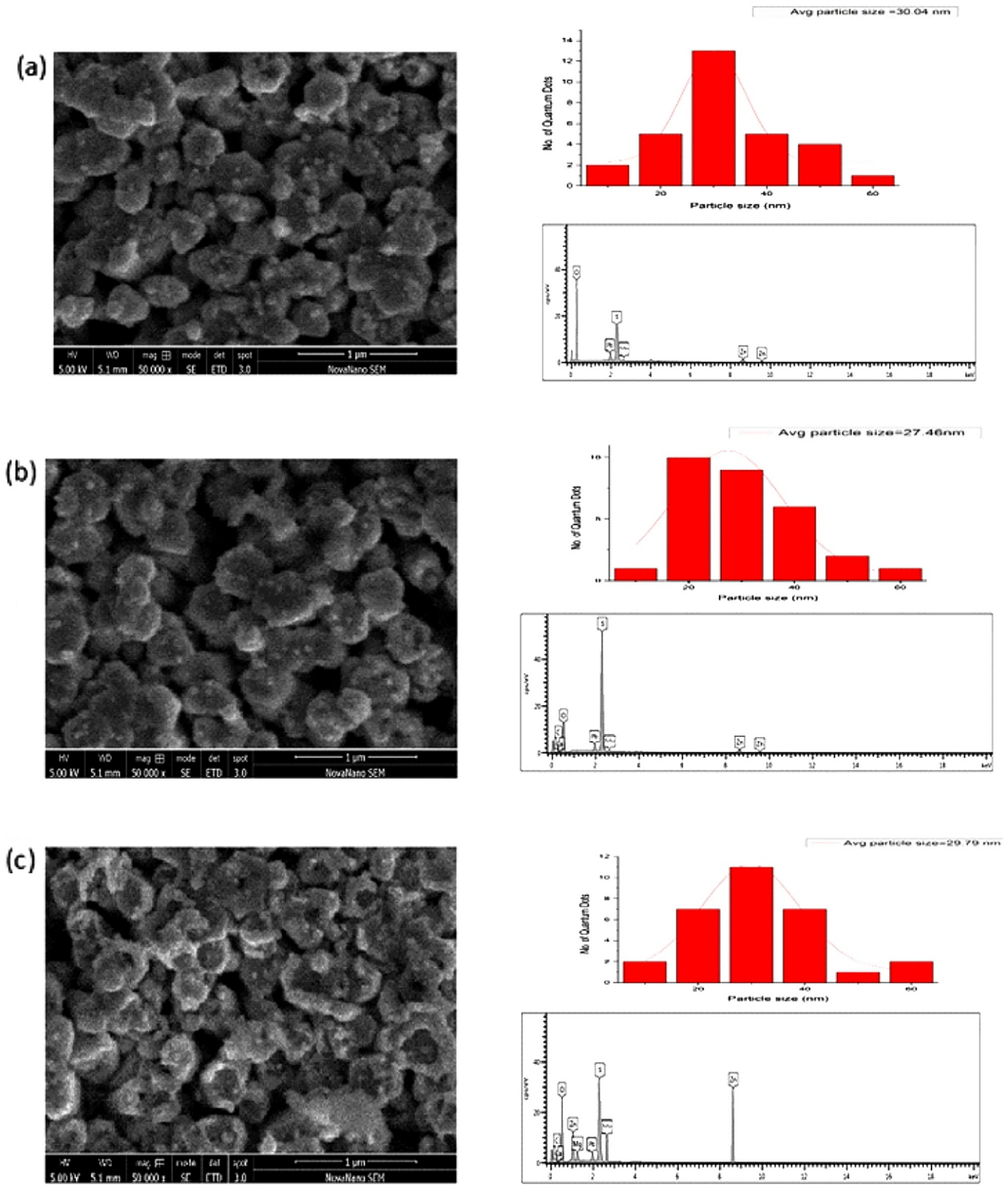

Fig. 4. (a, b and c) SEM and EDX analysis three working electrodes 1, 2 and 3 with MoO_3 deposited on PbS QDs/ZnO nanorods/FTO Glass at 100 °C , 150 °C and 200 °C respectively.

electrodes. The peaks obtained using EDS analysis show that the fabricated samples contain Zn, O, Pb, S and Mo. All samples are pure and contain only minor impurities. XRD and EDS data confirm the presence of all the materials synthesized.

SEM images show the uniform deposition of MoO_3 layer on PbS QDs sensitized ZnO nanorods grown on FTO glass. The average particle size of the synthesized QDs for all three samples was also calculated using the SEM micrographs. With the increase in temperature the crystallinity of PbS and MoO_3 has improved. SEM micrographs show the successful growth of ZnO nanorods, Pb QDs and MoO_3 layer.

It can be seen in the SEM images that the film which was annealed under 100 °C is quite uneven and clustered. However, it is also observed that the surface is much uniform when annealed at 150 °C. This is due to the evaporation of the solvent and the thin film formation of the MoO_3 under the increased temperature. The thermal treatment of the MoO_3 layers under this temperature makes the film more compact

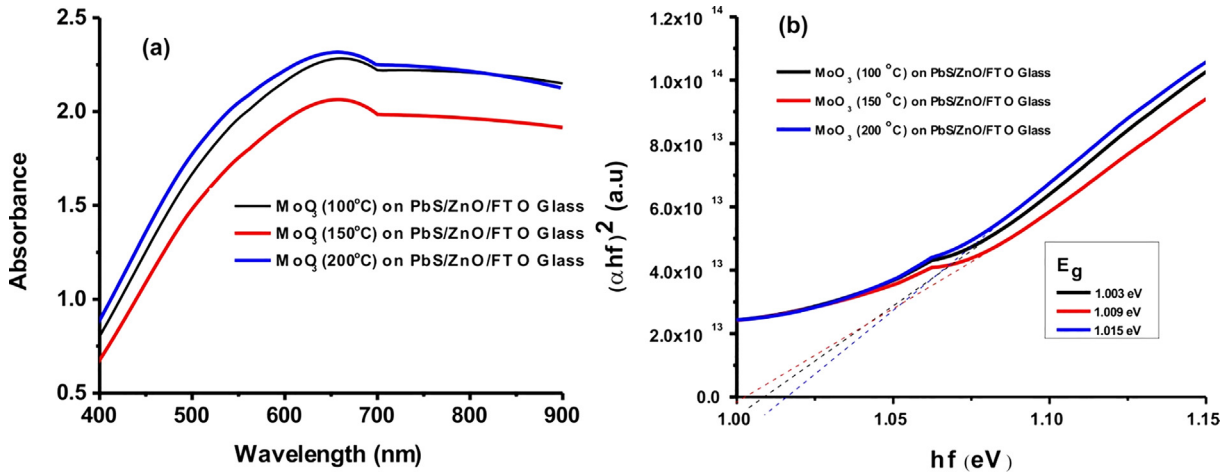

Fig. 5. (a) UV–Visible spectra and (b) Band gap analysis of three working electrodes 1, 2 and 3 with MoO_3 deposited on PbS QDs/ZnO nanorods/FTO Glass at 100 °C, 150 °C and 200 °C respectively.

which results in leakage free solar cells and is also favorable to the device improvement. Furthermore, raising the annealing temperature to 200 °C results in the multiple diffusion of the smaller particles which gather together to form larger grains. This makes the MoO_3 film less uniform and more clustered. The MoO_3 layer which is heated at 150 °C shows the optimal surface smoothness and density which blocks the leakage current and prevents shorts which is important for its implementation in solar cells.

3.3. Optical absorption of photo anodes

Fig. 5(a) shows the UV–VIS optical absorption spectra of MoO_3 coated PbS /ZnO/FTO Glass, working electrodes1, 2 and 3 with MoO_3 annealing temperature 100 °C, 150 °C and 200 °C respectively. It is evident from the figure that each spectrum shows a broad absorption in the visible range. It can be observed for Fig. 4a that the overall optical absorption in the visible region for each working electrode is increased by increasing the MoO_3 annealing temperature.

The maximum absorption for MoO_3 (100 °C) on PbS/ZnO/FTO Glass, MoO_3 (150 °C) on PbS/ZnO/FTO Glass and MoO_3 (200 °C) on PbS/ZnO/FTO Glass is 2.28 at 662 nm, 2.06 at 658 nm and 2.31 at 658 nm respectively as show in Table 2.

The absorption spectra of PbS QDs show that PbS QDs can harvest solar energy mainly in 600–900 nm indicating that devices display a broad light absorption from the visible to the near infra-red (NIR) region. Fig. 5(b) shows corresponding values of energy band gap for MAM on PbS QDs/ZnO nanorods/FTO Glass with first MoO_3 layer annealing temperature 100 °C, 150 °C and 200 °C were 1.003 eV, 1.009 eV and 1.015 eV respectively (seeTable 2).

The optical absorption of MoO_3 thin film can be affected by its morphology. From SEM analysis it is observed that annealing temperature effects morphology of thin films. MoO_3 thin film which is annealed at 100 °C has rough surface as compared that annealed at 150 °C. When annealing temperature is further increased to 200 °C larger grains are formed as a result of diffusion of smaller particles and surface of MoO_3 thin film became rough. As uniformity of thin film gets varied with annealing temperature the porosity as well as surface area has also changed. Uniform thin film with low porosity and surface area resulted in lower absorption of light. On the other hand thin films with rough surface, having high porosity, have large surface area. Large surface area of thin film thus allows stronger absorption (Borah et al., 2019). That's why the thin film of MoO_3 annealed at 200 °C having large surface area due to rough surface shows stronger absorption of light. While MoO_3 thin film which was annealed at 150 °C with less porous and uniform surface shows relatively lower optical absorption. The thin film of MoO_3 which was annealed at 100 °C shows higher absorption than MoO_3 film annealed at 150 °C. This is because MoO_3 thin film obtained as a result of annealing at 100 °C has rough surface due to which its surface area is large and it allows more absorption of light.

Table 2
Optical Properties of Working electrode 1, 2 and 3.

Temp of MoO_3 (°C)	Maximum absorption (a.u)	Absorbance peak (nm)	Bandgap (eV)
100	2.28	662	1.003
150	2.06	658	1.005
200	2.31	658	1.015

3.4. Photovoltaic performance

The performance of all three devices can be seen inTable 3 . J-V curves of device are also depicted in Fig. 6. The device annealed at 100 °C shows a PCE of 3.7% with a short-circuit current density (Jsc) of 5.207 mA cm^{-2}, an open-circuit voltage (Voc) of 0.790 V, and a fill factor (FF) of 89%. In contrast, the four parameters (Voc, Jsc, FF, and PCE) of devices with the MAM electrode reveal different types of results when annealed from 150 °C to 200 °C.

The device which was annealed at 150 °C shows the best PCE OF 4.6%, with a Voc of 0.796 V, a Jsc of 6.525 mA cm^{-2}, and a FF of 89%. The device performance has decreased when it is further annealed at 200 °C with a PCE of 3.9%, a Voc of 0.796 V, a Jsc of 5.591 mA cm^{-2}, and a FF of 87%.

The improved PCE of the device is associated with the fact that the film was most dense and compact when annealed at 150 °C. It can be seen from the SEM images that the film heated at 100 °C is not so smooth and small grains of MoO_3 are noticed on the surface which leads to poor device performance. However, the surface becomes much smoother and compacter when the annealing temperature is raised to 150 °C, with reduced charge recombination and a lower leakage current that is caused by the film roughness. But, a certain amount of roughness

Table 3
The performance parameters of device 1, 2 and 3.

Back Electrode	Voc (V)	J_{sc} (mA cm^{-2})	FF	PCE (%)
MAM (100 °C)	0.790	5.207	0.89	3.7
MAM (150 °C)	0.794	6.525	0.89	4.6
MAM (200 °C)	0.796	5.591	0.87	3.9

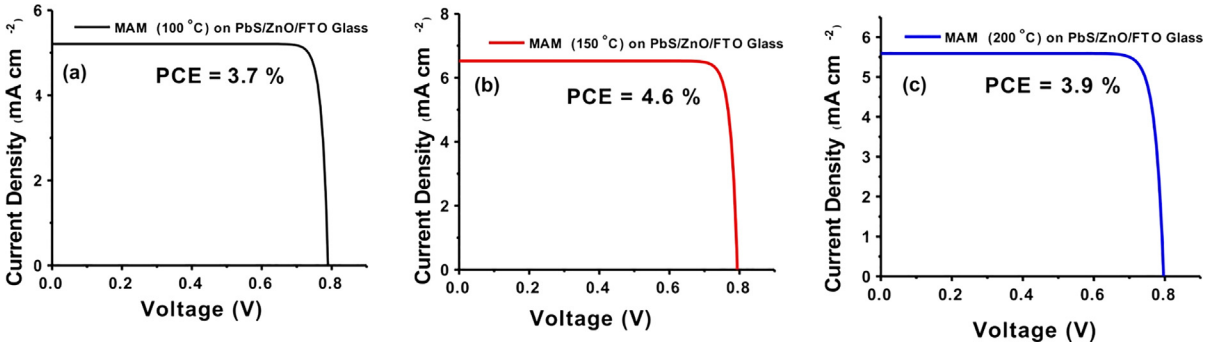

Fig. 6. J-V curves of MAM (100 °C) on PbS QDs/ZnO nanorods/FTO Glass, MAM (150 °C) on PbS QDs/ZnO nanorods/FTO Glass and MAM (200 °C) on PbS QDs/ZnO nanorods/FTO Glass.

is observed in the film when the temperature was raised to 200 °C, increasing the temperature resulted in a slight aggregation of particles which made the film rougher.

4. Conclusion

Annealing temperature inner MoO_3 played important role for structural and optical properties of working electrode. With the increase in temperature the crystallinity of PbS and MoO_3 was improved and increase in bandgap of the working electrode was also evident. The device which was annealed at 150 °C showed the best performance with the PCE of 4.617%. It is found that the performance of the QDSC depends strongly on the annealing temperature of the MoO_3 layer and shows the best results at 150 °C. In conclusion, the device structure that we have reported is a viable candidate for the QDSC.

Declaration of Competing Interest

The authors declare that they have no known competing financial interests or personal relationships that could have appeared to influence the work reported in this paper.

References

Borah, D.J., Mostako, A.T.T., Saikia, P.K., Dutta, P., 2019. Effect of thickness and post deposition annealing temperature on the structural and optical properties of thermally evaporated molybdenum oxide films. Mater. Sci. Semicon. Proc. 93, 111–122.
Carey, G.H., Abdelhady, A.L., Ning, Z., Thon, S.M., Bakr, O.M., Sargent, E.H., 2015. Colloidal quantum dot solar cells. Chem. Rev. 115, 12732–12763.
Gao, J., Perkins, C.L., Luther, J.M., Hanna, M.C., Chen, H.Y., Semonin, O.E., Beard, M.C., 2011b. n-Type transition metal oxide as a hole extraction layer in PbS quantum dot solar cells. Nano Lett. 11, 3263–3266.
Gao, J., Luther, J.M., Semonin, O.E., Ellingson, R.J., Nozik, A.J., Beard, M.C., 2011a. Quantum dot size dependent J− V characteristics in heterojunction ZnO/PbS quantum dot solar cells. Nano Lett. 11, 1002–1008.
Ibupoto, Z., Khun, K., Eriksson, M., AlSalhi, M., Atif, M., Ansari, A., Willander, M., 2013. Hydrothermal growth of vertically aligned ZnO nanorods using a biocomposite seed layer of ZnO nanoparticles. Mater. 6, 3584–3597.
Jean, J., Brown, P.R., Jaffe, R.L., Buonassisi, T., Bulović, V., 2015. Pathways for solar photovoltaics. Energy Environ. Sci. 8, 1200–1219.
Jo, J.W., Kim, Y., Choi, J., de Arquer, F.P.G., Walters, G., Sun, B., Fan, J., 2017. Enhanced open-circuit voltage in colloidal quantum dot photovoltaics via reactivity-controlled solution-phase ligand exchange. Adv. Mater. 29, 1703627.
Kang, R., Park, S., Jung, Y.K., Lim, D.C., Cha, M.J., Seo, J.H., Cho, S., 2018. High-efficiency polymer homo-tandem solar cells with carbon quantum-dot-doped tunnel junction intermediate layer. Adv. Energy Mater. 8, 1702165.
Kramer, I.J., Sargent, E.H., 2011. Colloidal quantum dot photovoltaics: a path forward. ACS Nano 5, 8506–8514.
Lan, X., Masala, S., Sargent, E.H., 2014. Charge-extraction strategies for colloidal quantum dot photovoltaics. Nat. Mater. 13, 233.
Lee, J.W., Son, D.Y., Ahn, T.K., Shin, H.W., Kim, I.Y., Hwang, S.J., Park, N.G., 2013. Quantum-dot-sensitized solar cell with unprecedentedly high photocurrent. Sci. Rep. 3, 1050.
Li, H., Jiao, S., Bai, S., Li, H., Gao, S., Wang, J., Zhao, L., 2014. Precursor-controlled synthesis of different Zn O nanostructures by the hydrothermal method. Phys. Status Solidi A 211, 595–600.
Li, H., Jiao, S., Li, H., Li, L., Zhang, X., 2015. Tunable growth of PbS quantum dot–ZnO heterostructure and mechanism analysis. CrystEngComm 17, 4722–4728.
Li, Y., Yu, H., Huang, X., Wu, Z., Chen, M., 2017. A simple synthesis method to prepare a molybdenum oxide hole-transporting layer for efficient polymer solar cells. RSC Adv. 7, 7890–7900.
Luther, J.M., Gao, J., Lloyd, M.T., Semonin, O.E., Beard, M.C., Nozik, A.J., 2010. Stability assessment on a 3% bilayer PbS/ZnO quantum dot heterojunction solar cell. Adv. Mater. 22, 3704–3707.
McCarron III, E.M., Calabrese, J.C., 1991. The growth and single crystal structure of a high pressure phase of molybdenum trioxide: MoO3-II. J. Solid State Chem. 91, 121–125.
Mustakim, N.S.M., Ubani, C.A., Sepeai, S., Ludin, N.A., Teridi, M.A.M., Ibrahim, M.A., 2018. Quantum dots processed by SILAR for solar cell applications. Sol. Energy 163, 256–270.
Nafees, M., Ikram, M., Ali, S., 2017. Thermal stability of lead sulfide and lead oxide nanocrystalline materials. Appl. Nanosci. DFRS7, 399–406.
Nozik, A.J., 2008. Multiple exciton generation in semiconductor quantum dots. Chem. Phys. Lett. 457, 3–11.
Park, H., Chang, S., Jean, J., Cheng, J.J., Araujo, P.T., Wang, M., Gradečak, S., 2012. Graphene cathode-based ZnO nanowire hybrid solar cells. Nano Lett. 13, 233–239.
Rühle, S., Shalom, M., Zaban, A., 2010. Quantum-dot-sensitized solar cells. ChemPhysChem 11, 2290–2304.
Samadpour, M., Jun, H.K., Parand, P., Najafi, M.N., 2019. CdS quantum dots pre-deposition for efficiency enhancement of quantum dot-sensitized solar cells. Sol. Energy 188, 825–830.
Sun, W., Jha, J.K., Shepherd, N.D., Du, J., 2018. Interface structures of ZnO/MoO3 and their effect on workfunction of ZnO surfaces from first principles calculations. Comput. Mater. Sci. 141, 162–169.
Tao, C., Xie, G., Liu, C., Zhang, X., Dong, W., Meng, F., Chen, W., 2009. Semitransparent inverted polymer solar cells with MoO 3/Ag/MoO 3 as transparent electrode. App. Phys. Lett. 95, 206.
Tian, J., Shen, T., Liu, X., Fei, C., Lv, L., Cao, G., 2016. Enhanced performance of PbS-quantum-dot-sensitized solar cells via optimizing precursor solution and electrolytes. Sci. Rep. 6, 23094.
Wang, H., Kubo, T., Nakazaki, J., Kinoshita, T., Segawa, H., 2013. PbS-quantum-dot-based heterojunction solar cells utilizing ZnO nanowires for high external quantum efficiency in the near-infrared region. J. Phys. Chem. Lett. 4, 2455–2460.
Yang, Y., Chen, Q., Hsieh, Y.T., Song, T.B., Marco, N.D., Zhou, H., Yang, Y., 2015. Multilayer transparent top electrode for solution processed perovskite/Cu In, Ga Se, S 2 four terminal tandem solar cells. ACS Nano 9, 7714–7721.
Yao, D.D., Ou, J.Z., Latham, K., Zhuiykov, S., O'Mullane, A.P., Kalantar-zadeh, K., 2012. Electrodeposited α-and β-phase MoO3 films and investigation of their gasochromic properties. Cryst. Growth Des. 12, 1865–1870.
Zhang, J., Gao, J., Church, C.P., Miller, E.M., Luther, J.M., Klimov, V.I., Beard, M.C., 2014. PbSe quantum dot solar cells with more than 6% efficiency fabricated in ambient atmosphere. Nano Lett. 14, 6010–6015.
Zhang, X., Hägglund, C., Johansson, M.B., Sveinbjörnsson, K., Johansson, E.M., 2016. Fine tuned nanolayered metal/metal oxide electrode for semitransparent colloidal quantum dot solar cells. Adv. Funct. Mater. 26, 1921–1929.